buildings

MDPI

Article

Numerical Study on the Seismic Behavior of Steel–Concrete Composite Frame with Uplift-Restricted and Slip-Permitted (URSP) Connectors

Zhenhao Wu [1,2], Xin Nie [2], Jizhi Zhao [3], Wei Wang [2] and Linli Duan [1,*]

[1] School of Civil Engineering, Central South University, Changsha 410075, China; zhenhaowu21@163.com
[2] Key Laboratory of Civil Engineering Safety and Durability of China Education Ministry, Department of Civil Engineering, Tsinghua University, Beijing 100084, China; xinnie@tsinghua.edu.cn (X.N.); wang_wei_thu@126.com (W.W.)
[3] School of Civil Engineering, Chongqing University, Chongqing 400044, China; 13120084917@163.com
* Correspondence: linliduan@csu.edu.cn

Abstract: Uplift-restricted and slip-permitted (URSP) connectors have been demonstrated to effectively enhance the anti-cracking performance of RC slabs in negative moment areas. While their efficacy is recognized, studies of composite frames utilizing URSP connectors remain scarce, limiting their application in construction. This research undertakes a numerical analysis of the seismic performance of steel–concrete composite frames that employ URSP connectors. The influence of key design parameters on seismic behavior is scrutinized. Leveraging prior tests on composite frames with URSP connectors carried out by the authors' group, a sophisticated three-dimensional FEM model is crafted. This model, built using the ABAQUS software (2016), accounts for the intricate mechanical behaviors of shear connectors. The fidelity of the FEM model is validated through a juxtaposition of numerical and test outcomes, assessing strain distribution, damage patterns, and load–displacement curves. This numerical model serves as a basis for the study, exploring the impacts of three crucial design parameters on structural seismic performance. The findings suggest that the arrangement length of URSP connectors should be constrained to less than half of the frame beam's span to optimize mechanical performance during seismic events. Additionally, enhancing both the flange thickness and the steel beam's height is recommended to further bolster structural integrity.

Keywords: steel–concrete composite frame; URSP connectors; numerical study; parametric analysis; seismic performance

Citation: Wu, Z.; Nie, X.; Zhao, J.; Wang, W.; Duan, L. Numerical Study on the Seismic Behavior of Steel–Concrete Composite Frame with Uplift-Restricted and Slip-Permitted (URSP) Connectors. *Buildings* **2023**, *13*, 2598. https://doi.org/10.3390/buildings13102598

Academic Editor: Elena Ferretti

Received: 20 September 2023
Revised: 9 October 2023
Accepted: 12 October 2023
Published: 14 October 2023

1. Introduction

A steel–concrete composite frame is composed of composite beams and columns, and is interconnected by composite joints. Numerous studies and practical engineering applications have confirmed that composite frames capitalize on the mechanical benefits of both concrete and steel [1–5]. In comparison to an exclusive steel frame, an RC slab and steel beam collaboratively function via shear connectors, bolstering structural load-bearing capacity and augmenting lateral stiffness. Additionally, the RC slab distributes the load to the top flange, resulting in a decrease in the steel required for the structure. On the other hand, when compared to reinforced concrete frames, composite frames significantly reduce the structure's overall weight, leading to a reduced seismic response. Further, the sectional dimensions of the composite frame are more compact, enhancing the usable space within buildings. Notably, the steel components can function as construction platforms and supports, eliminating the need for comprehensive scaffolding and formwork and thus expediting the construction timeline [6,7].

However, in areas of negative moments, susceptibility to cracking can adversely impact the structural behavior and durability, hindering the broader adoption and popularization of composite structures [8,9]. Conventional anti-cracking approaches, such as

the prestressing method and the group stud method [10–12], have seen widespread use in engineering projects to mitigate the cracking risk of the RC slab. However, these methods present complexities in the configuration of the concrete slab. Both the effectiveness of these techniques and their overall structural integrity leave room for improvement.

In response, a novel type of shear connector for composite structures, termed the uplift-restricted and slip-permitted (URSP) connector (including screw-type, T-shape type, and slip-type), was introduced based on the foundational principles of composite structures by Nie et al. [13]. These connectors proficiently diminish the tensile stress of the RC slab by allowing for interface shear flexibility, while maintaining the uplift resistance between the steel and the RC slab. When juxtaposed with conventional crack-control methods, this innovative approach offers the benefits of straightforward detailing, ease of implementation, and cost-effectiveness. Furthermore, the utilization of URSP connectors results in a marked increase in plastic slip between the concrete slab and the steel beam. This escalation not only augments the ductility of the composite frames but also enhances their energy dissipation capabilities, as corroborated by references [14,15]. Following the introduction of the URSP connectors, several studies have investigated their slip and uplift characteristics, leading to the proposal of a shear–slip model [16–18].

Continued exploration of the URSP connectors' impact on the mechanical performance of composite structures has garnered significant attention from researchers. Notably, Nie et al. conducted experiments on scale models of composite truss bridges employing both traditional shear studs and URSP connectors [19]. A comparative analysis found that while the initial stiffness and negative moment capacity of the composite bridge remained relatively stable, there was a marked increase in the cracking load. Han introduced design methodologies and recommendations for composite beams incorporating URSP connectors, amalgamating experimental research, numerical analyses, and existing design methods [20]. Similarly, Li and Ma et al. undertook a numerical examination of the mechanical behavior of a three-span continuous steel–concrete composite bridge fitted with URSP connectors [21,22]. Their findings underscored the fact that this novel connector type could reduce tensile stresses in the RC slab by moderating the composite action between the steel beam and the RC slab, leading to the introduction of actionable design and construction techniques. Furthermore, Nie et al. performed quasi-static tests on composite frames featuring URSP screw-type connectors to evaluate the effect of connector type and the arrangement length of the URSP connectors on the structure's mechanical properties [23]. These tests revealed that compared to specimens utilizing full-span URSP connectors, those equipped with half-span URSP connectors exhibited superior seismic performance, including enhanced ductility and lateral elastic stiffness.

While prior studies have predominantly centered on the incorporation of URSP connectors into composite girders and bridges, with notable applications in practical bridge engineering (for instance, the Tianjin Haihe Road and Majiahu Overpass in China), there remains a gap in understanding their advantages within composite frames. The limited existing experimental research on composite frames equipped with URSP connectors has yet to comprehensively reveal the potential advantages associated with these configurations. Additionally, given that large-scale experimental research is both time-intensive and laborious, it is challenging to quantitatively ascertain the specific impact of each design parameter on seismic performance through experimental means alone. In the present study, we undertook a numerical investigation of the composite frame employing URSP connectors. This work scrutinized the effects of pivotal design parameters on both the mechanical and anti-crack capabilities. Initially, a detailed FEM model of test specimen CF2, as described by Nie et al., was built using the ABAQUS software [23]. By juxtaposing this model with empirical test results, the reliability and precision of the FEM model were authenticated. Leveraging insights obtained from the validated model, we further explored the implications of three prominent design parameters: the arrangement length of URSP connectors, the flange thickness of the steel beam, and the steel beam height. Our aim

was to demonstrate their respective contributions to augmenting the structure's seismic resilience. Based on our findings, pertinent design recommendations are made.

2. Numerical Investigation

2.1. Numerical Model

The finite-element model for specimen CF2 primarily comprises two major components: the CFST column H-steel beam frame and the concrete slab. The modeling strategies for each are detailed below.

2.1.1. CFST Column H-Steel Beam Frame

A nonlinear FEM model for the CFST column H-steel beam frame was established, as illustrated in Figure 1. Extensive simulation results indicate that the shell element is effective at simulating the deformation and stress of thin-walled components both accurately and efficiently [4,24,25]. Therefore, the steel plates of the CFST columns and steel beams, a four-node quadrilateral linear reduced-integration shell element (labeled S4R in the Abaqus element library) was employed. Meanwhile, the concrete within the CFST columns was represented using an 8-node hexahedral linear reduced-integration solid element (referred to as the C3D8R element). Grid test results indicated that when the grid size was set to under 50 mm (equivalent to half of the beam flange's length), the simulation outcomes remained consistent. Hence, the grid size selected for the frame was between 25 and 50 mm, balancing both accuracy and computational efficiency. Additionally, the region near the beam ends was suitably refined to ensure precision.

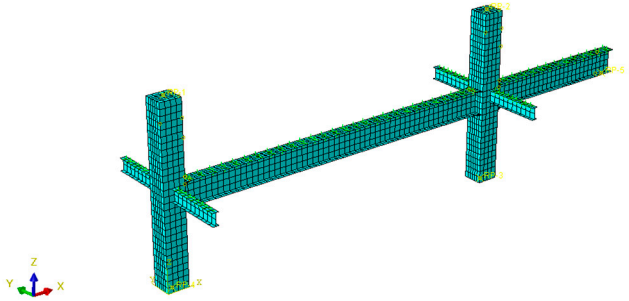

Figure 1. Mesh detailing of the CFST column H-steel beam frame.

2.1.2. RC Slab

The reinforced concrete (RC) slab was bifurcated into two primary components: the concrete itself and its embedded reinforcement. The reinforcing bars, housed within the concrete, function synergistically with it, enabled by bonding anchorage. Given that bond anchorage was not the primary focal point of this investigation, a layered four-node quadrilateral linear reduced-integration shell element (denoted as the layered S4R element in the Abaqus element library) was utilized for its computational efficiency in simulating the reinforced concrete slab, rather than a more intricate solid-truss model, as depicted in Figure 2. The stratified composition of the shell, encompassing the concrete, longitudinal rebars, and transverse rebars, was delineated using Abaqus's layered materials feature, as showcased in Figure 3. Based on the equivalent area comparison between the reinforcement bars of the test specimen and the layered shell, the specific thickness (or proportion) attributed to each reinforcement layer was ascertained. Details of this are provided in Table 1. Grid test outcomes suggested that maintaining a grid size under 50 mm was paramount for simulation stability. Thus, to enhance computational performance, the grid size chosen for the RC slab was set at 50 mm.

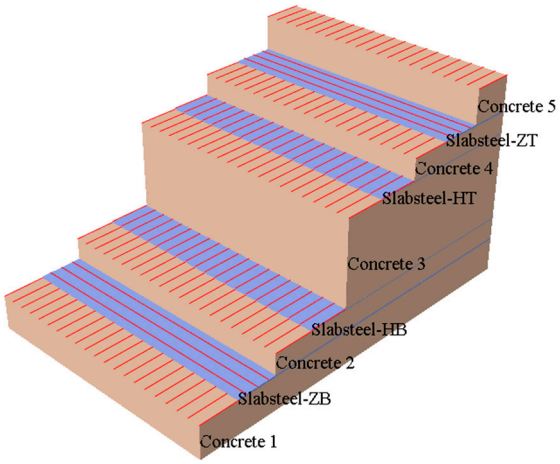

Figure 2. Layered shell model of the concrete slab.

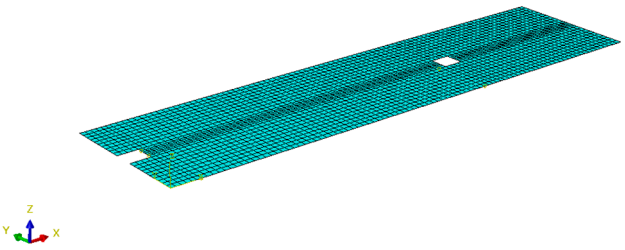

Figure 3. Model meshing of the concrete slab.

Table 1. The proportion of each layer of the RC slab in the finite-element model.

Ply Number	Material	Thickness (Proportion)
1	Concrete	10.02 (16.7%)
2	Transverse reinforcement	0.50 (0.84%)
3	Concrete	6.22 (10.36%)
4	Longitudinal reinforcement	0.28 (0.47%)
5	Concrete	25.96 (43.26%)
6	Longitudinal reinforcement	0.28 (0.47%)
7	Concrete	6.22 (10.36%)
8	Transverse reinforcement	0.50 (0.84%)
9	Concrete	10.02 (16.7%)
Sum		60 (100%)

Unit: mm.

2.1.3. Connection Simulation

The tie connection method was utilized to simulate the interaction between the filled concrete and the rectangular tube-steel within the CFST columns. This approach had a minimal impact on the structural mechanical performance and was also validated in a prior study [26].

In specimen CF2, both shear studs and URSP connectors were affixed to the top flange of the steel beam. To reproduce their mechanical behavior, fastener constraints were implemented at the interface, corresponding to the connectors' position between the RC slab and the steel beam. These fasteners maintained a physical radius of 5 mm, consistent with the experimental design. Based on the loading characteristics observed in the experiment, these fastener constraints were characterized as slots. Consequently, degrees of freedom in both the Z-direction and Y-direction were restrained, while freedom in the X-direction (parallel to the steel beam's longitudinal axis) remained unrestricted.

The nonlinear force-deformation characteristics for the connectors in the X-direction were defined according to the shear–slip models of both the shear studs and the URSP connectors.

The shearing behavior of the shear studs was represented using the shear–slip curve as proposed by Ollgard [27], depicted in Figure 4 and defined by Equation (1).

$$V = V_{\mathrm{u}}\left(1 - e^{-\mathrm{n}s}\right)^{\mathrm{m}} \tag{1}$$

where V represents the shear force, V_{u} stands for the ultimate shear capacity, and s is the interfacial slip. The value of V_{u} is ascertained based on the related formulas in the "Code for Design of Composite Structures (JGJ138-2016)" [28]. As suggested in [27], m = 0.558, n = 1 mm^{-1}.

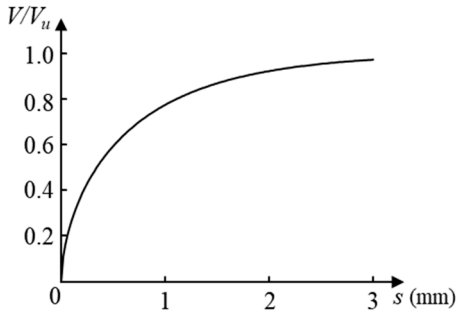

Figure 4. Shear–slip model of the shear stud.

The shear–slip curve for URSP connectors, as shown in Figure 5, was used for the simulation on the complex mechanical behavior of the URSP connectors along the composite beam axis. Equations (2)–(5) are applied for calculating the shear force under arbitrary slip of the URSP connectors.

$$V = \begin{cases} k_0\delta & \delta \le \delta_0 \\ k_0\delta_0 & \delta_0 < \delta \le \frac{t_{\mathrm{s}}}{3} \\ V_{\mathrm{u}}\left[1 - e^{-\left(\delta - \frac{t_{\mathrm{s}}}{3}\right)}\right]^{0.558} + k_0\delta_0 \le V_{\mathrm{u}} & \frac{t_{\mathrm{s}}}{3} < \delta \le \delta_{\mathrm{u}} \\ V_{\mathrm{u}}\left[1 - \frac{\delta - \delta_{\mathrm{u}}}{10(\delta_{\mathrm{f}} - \delta_{\mathrm{u}})}\right] & \delta_{\mathrm{u}} < \delta < \delta_{\mathrm{f}} \end{cases} \tag{2}$$

$$V_{\mathrm{u}} = 0.43A_{\mathrm{s}}\sqrt{E_{\mathrm{c}}f_{\mathrm{c}}} \le 0.7A_{\mathrm{s}}\gamma f_{\mathrm{s}} \tag{3}$$

$$\frac{\delta_{\mathrm{u}}}{d_{\mathrm{s}}} = 0.41 - 0.0030f_{\mathrm{c}} + \frac{t_{\mathrm{s}}}{3d_{\mathrm{s}}} \tag{4}$$

$$\frac{\delta_{\mathrm{f}}}{d_{\mathrm{s}}} = 0.45 - 0.0021f_{\mathrm{c}} + \frac{t_{\mathrm{s}}}{3d_{\mathrm{s}}} \tag{5}$$

where δ and δ_0 denote the interfacial slip and the slip correlated to the interfacial bond failure, respectively. δ_{u} represents the slip which occurs at maximum capacity; δ_{f} constitutes the slip occurring at failure. k_0 indicates the stiffness level prior to the failure of the interfacial bond; t_{s} is representative of the foamed plastic thickness; A_{s} denotes the screw area; d_{s} is the screw's diameter. V stands for the shear force, while V_{u} represents ultimate shear capacity. Furthermore, E_{c} and f_{c} denote the modulus relevant to the elasticity and compressive strength of the concrete, respectively. Lastly, f_{s} denotes screw material yield strength.

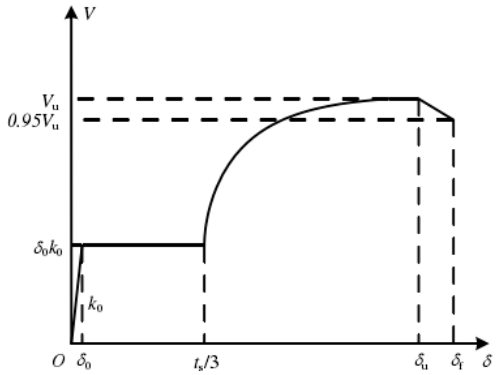

Figure 5. Shear–slip model of the URSF connector.

2.1.4. Material Constitutive Model

The uniaxial stress–strain model proposed by Esmaeilly and Xiao was adopted for modeling the mechanical behavior of the steel plate, as depicted in Figure 6 [29]. The mathematical expression can be ascertained from Equation (6).

$$\sigma = k_3 f_y + \frac{E_s(1-k_3)}{\varepsilon_y(k_2-k_1)^2}(\varepsilon - k_2\varepsilon_y)^2 \quad (6)$$

where f_y and E_s denote the yield strength and the modulus of elasticity of the steel, respectively. Both can be determined from the material property test results. ε_y represents the yield strain, while k_1, k_2, and k_3 are parameters controlling the shape of the curve. As recommended in [29], k_1 = 12, k_2 = 120, and k_3 = 1.2. The uniaxial hysteretic rules of steel draw upon the research by Tao et al. [30]. These rules depict a relatively straightforward unloading behavior, characterized by linear unloading based on the steel's modulus of elasticity (E_s). In contrast, the reloading behavior is more complex, determined by a p-curve as recommended by Légeron [31], which accounts for the Bauschinger effect.

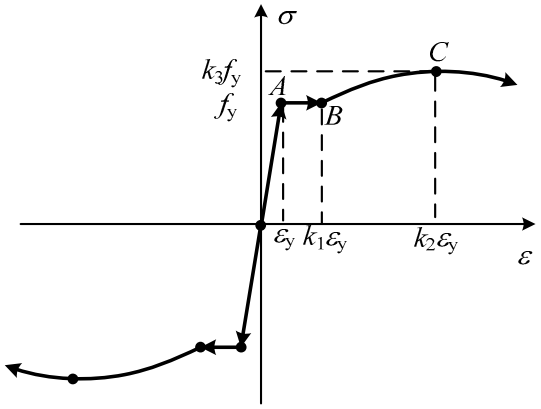

Figure 6. Uniaxial stress–strain model of steel.

The concrete damaged plasticity (CDP) model is commonly used in concrete simulations. The fundamental parameters of this model, including the modulus of elasticity, Poisson ratio, compressive strength, and tensile strength, are determined by material test results in [23]. The key parameters of the CDP model are outlined as recommended in [32] and are displayed in Table 2.

Table 2. Key parameters of CDP model.

Ψ	∈	α_f	***Kc***	***μ***
30°	0.1	1.16	0.667	0.005

In Table 2, Ψ and ∈ represent the dilation angle and eccentricity, respectively. Both parameters are instrumental in determining the flow rule. The symbol α_f denotes the ratio of concrete's biaxial compressive strength to its uniaxial compressive strength. *Kc* is employed to define the shape of the yield surface on the deviatoric plane. The viscosity parameter is represented by μ, which impacts the precision and convergence of the simulation. A larger μ value facilitates easier calculation convergence, while a smaller value yields more accurate simulation results.

The uniaxial stress–strain relationship of the concrete in CSFT columns is grounded in Han's research [33,34], which considers the enhancement effect on the mechanical performance of encased concrete caused by the passive restraining action exerted by the steel tube. The formulation expressing this stress–strain relationship is articulated based on the study referenced in [33,34]. The stress–strain relationship for the concrete slab adhered to the Code for Design of Concrete Structures (GB50010-2010) [35].

2.1.5. Boundary Condition

The boundary condition plays one of the most pivotal roles in influencing the accuracy of numerical results, as affirmed by two studies [36,37]. Figure 7 depicts the boundary conditions of the FEM model, mirroring the constraints observed in the actual experiment. The nodes at the bottom of the CFST columns restricted the degrees of freedom in all directions, excluding the rotational degree of freedom about the Y-axis, simulating the hinges. To replicate the impact of the vertical linking beam in the experiment, the degrees of freedom in both the Z-direction and Y-direction of the nodes on the beam end were constrained. Furthermore, the nodes' degree of freedom in the Y-direction at the top surface of the CFST column was limited to emulate the lateral supports for the columns in the experiment.

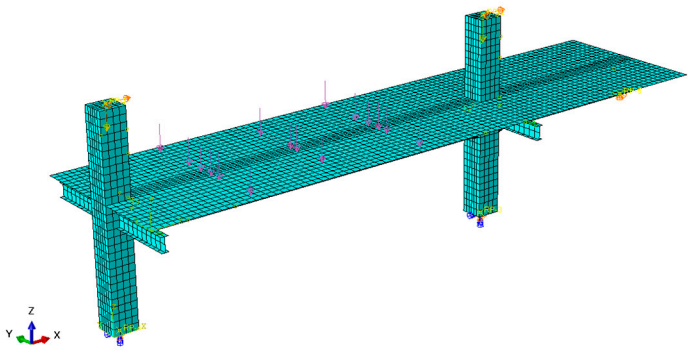

Figure 7. Boundary condition of the finite-element model.

2.1.6. Load Control

The loading protocol comprised two stages: vertical loading and lateral loading. This mirrored the actual conditions, as depicted in Figure 8. In the initial stage, vertical loads were applied to the RC slab, as shown in Figure 8a. Subsequently, axial loads of 150 kN and 300 kN, corresponding to axial compression ratios of 0.1 and 0.2, were consistently applied to the side and middle columns, respectively, which is depicted in Figure 8b. A lateral cyclic load, as demonstrated in Figure 8c, was then imposed on the top surface of both CFST columns.

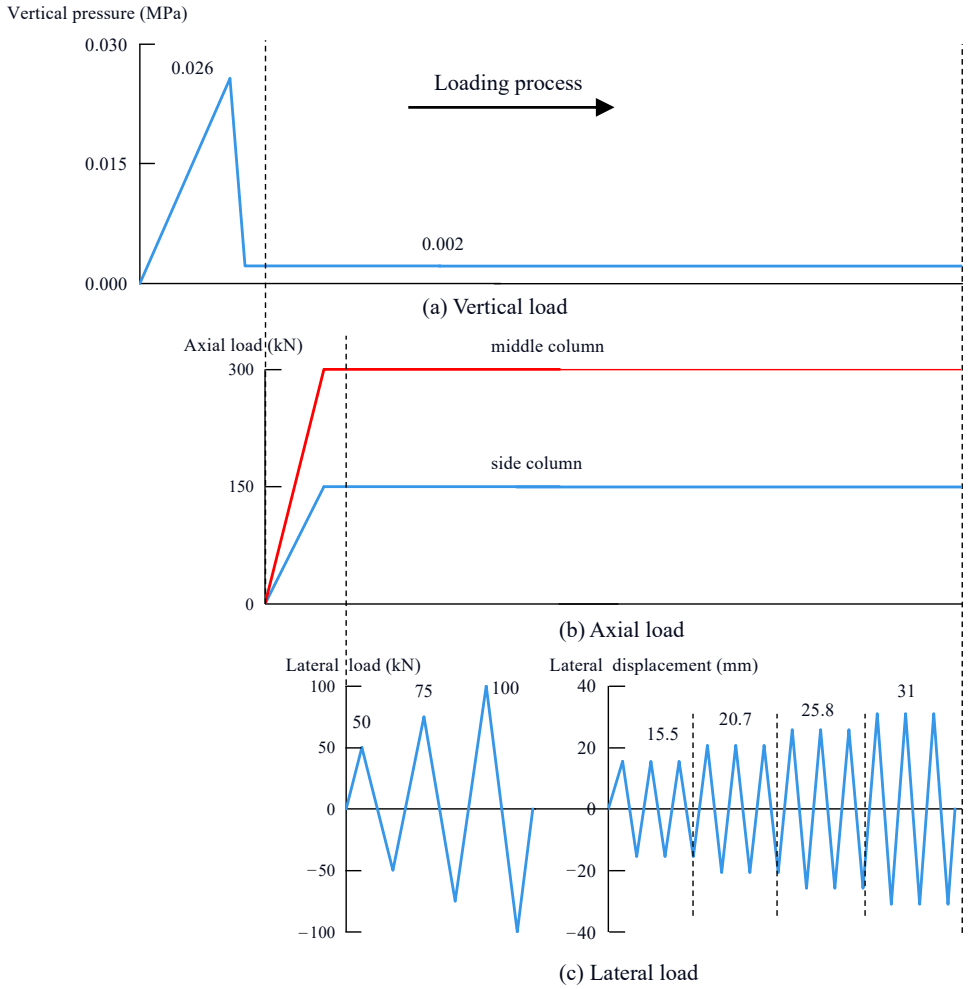

Figure 8. Loading protocol.

2.2. Model Verification

The accuracy of the FEM model is validated in this section by juxtaposing the results of the experiment with the numerical simulation [23].

Figure 9 illustrates the stress nephograms of CF2 at a displacement of 25.8 mm, a point at which the flange of the composite beam exhibits tearing damage in the experiment. The columns remain in the elastic stage since their maximum stress is 210 MPa, significantly below the yield stress. Areas with pronounced stress are primarily localized near the node at the beam end. This beam end, where stress is mostly concentrated, has entered the yield stage. This is evidenced by its maximum stress of 370 MPa, which surpasses the yield stress of steel. This suggests that a plastic hinge has formed at the beam end to dissipate incoming energy. The numerical results significantly align with the experimental results.

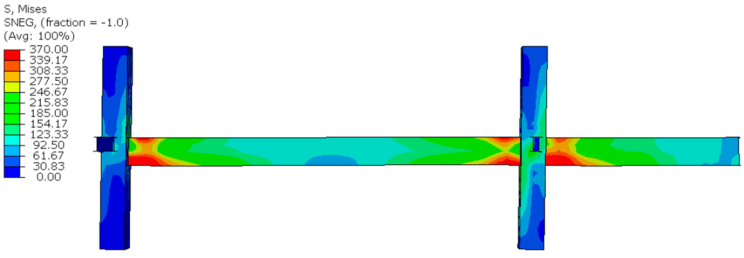

Figure 9. Stress distribution of the composite frame at a displacement of 25.8 mm.

Figure 10 juxtaposes the cracking damage distribution of the RC slab in the simulation results with the test results at a displacement of 25.8 mm. In the experimental results, it is depicted by the crack distribution diagram. It is important to note that the value of the concrete damage factor ranges from 0 to 1, with a higher value parameter indicating a more severe degree of tension cracking in the area. The similarity between the numerical and experimental results is evident. Most of the damage is localized at the beam end. Notably, the damage to the concrete slab in area B is more severe than that in another area, corroborating the findings from the experimental results.

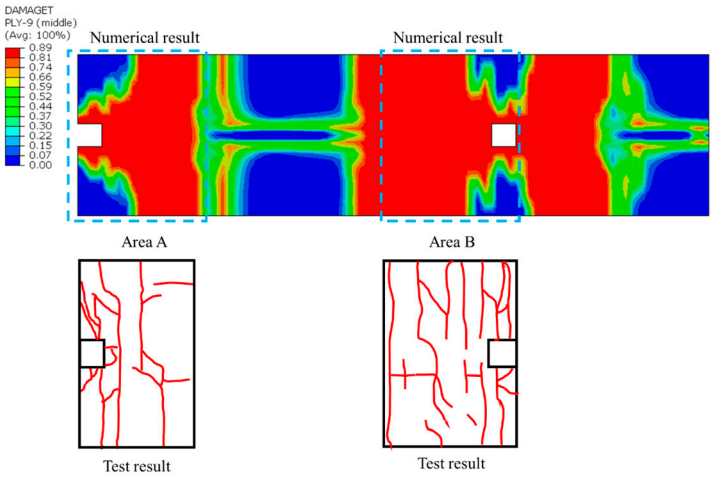

Figure 10. Concrete cracking damage distribution.

Figure 11 presents a comparison between the load–displacement curves of the FEM model and the test specimen. The simulation results align closely with the experimental findings. It is noteworthy that the composite beam's flange experiences tearing damage in the experiment at a displacement of 25.8 mm, after which the load in the experiment starts to decline. The FEM model does not account for the tearing damage of the steel flange, influencing the accuracy of the numerical model after the 25.8 mm displacement. However, given that the primary focus of this study revolves around the seismic behavior of the structure prior to failure, the hysteresis curve following the 25.8 mm displacement is not illustrated. Additionally, the forward loading capacity is slightly elevated compared to the reverse loading. This is attributed to the composite beam's positive moment capacity, which is substantially larger than its hogging moment capacity. During forward loading, two positive moments are observed, while reverse loading exhibits one positive moment at the three beam ends.

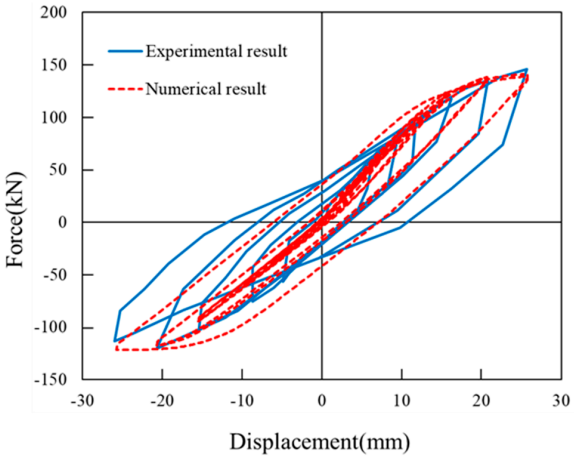

Figure 11. Comparison of hysteresis curves.

Table 3 presents a comparison of characteristic parameters, such as initial stiffness and ultimate load. These parameters, derived from the numerical model, are compared with those extracted from the experimental hysteresis curves. Both parameters have a discrepancy of less than 10%. This suggests that the modeling technique proposed in this study effectively captures the nonlinear mechanical behaviors of this structure prior to the onset of substantial tearing damage at the beam end.

Table 3. Comparison of mechanical characteristic parameters.

Specimen	Model	Positive Loading		Negative Loading	
		Elastic Stiffness (kN/mm)	Ultimate Load (kN)	Elastic Stiffness (kN/mm)	Ultimate Load (kN)
CF2	Experimental	11.9	151.2	8.4	123.2
	Numerical	10.8	145.0	7.7	122
	Ratio	0.91	0.96	0.92	0.99

3. Analysis of Design Parameters

Drawing from insights in prior studies [22,23], the primary determinants influencing the mechanical behaviors of composite frames using URSP connectors are the arrangement length of URSP connectors, the flange thickness of the steel beam, and the height of the steel beam. Notably, upon the integration of URSP connectors, the shear constraint between the steel beam and the RC slab is diminished, leading to a reduction in the tensile stress within the RC slab in areas of hogging moments. This change enhances the structure's resistance to cracking. Conversely, the elastic stiffness of the structure decreases, which is attributed to the disintegration of composite action on the composite beam by the URSP connectors. As a result, the RC slab and steel beam operate more as individual entities. Modifications in the flange thickness and the height of the steel beam alter the structure's seismic performance by adjusting the composite beam's bending moment of inertia. Specific values for each design parameter are detailed in Table 4. These were ascertained by either increasing or decreasing the parameters observed in specimen CF2. This section explores in greater depth the influence of these critical design parameters on the structure's seismic resilience.

Table 4. Design parameters.

Parameter	Value
Arrangement length of URSP connectors	$0.0L_0$, $0.25L_0$, $0.50L_0$, $0.75L_0$, $1.0L_0$
Flange thickness of steel beam	$0.75t_{w0}$, $1.0t_{w0}$, $1.5t_{w0}$, $1.75t_{w0}$, $2.0t_{w0}$
Steel beam height	$0.5h_0$, $0.75h_0$, $1.0h_0$, $1.13h_0$, $1.25h_0$

Note: L_0, t_{w0}, h_0 denote the half span of the composite beam of CF2, the flange thickness of the steel beam of CF2, and its height, respectively.

3.1. Arrangement Length of URSP Connectors

URSP connectors are strategically positioned on the steel beam's top flange, effectively easing the shear constraint between the RC slab and the top flange of the steel beam. However, this novel type of connector also undermines the composite action. An excessively extended arrangement length could cause the combined inertia moment of the RC slab and steel in this region to drop considerably, leading to a pronounced reduction in the frame's lateral stiffness. Thus, pinpointing an optimal arrangement length for URSP connectors is imperative.

Figure 12 presents the stress nephogram of the composite frame across varying URSP connectors' arrangement lengths at a drift ratio of 1/50 (equivalent to a displacement of 30.6 mm). This ratio corresponds to the threshold set for composite frames during significant seismic events as stipulated in the Code for Seismic Design of Buildings (GB 50011-2011) [38]. As observed from the figure, irrespective of the different L values, the beam end reaches the yield phase, while the stress within the CFST column remains at 200 MPa—a value considerably below the yield stress. As such, the structure adheres to the "strong column-weak beam" design principle. For URSP connector arrangement lengths of less than $0.5L_0$, the stress distribution within the steel frame remains largely unchanged. Beyond this point, as the arrangement length extends, both the stress magnitude and the yield zone at the beam end begin to wane.

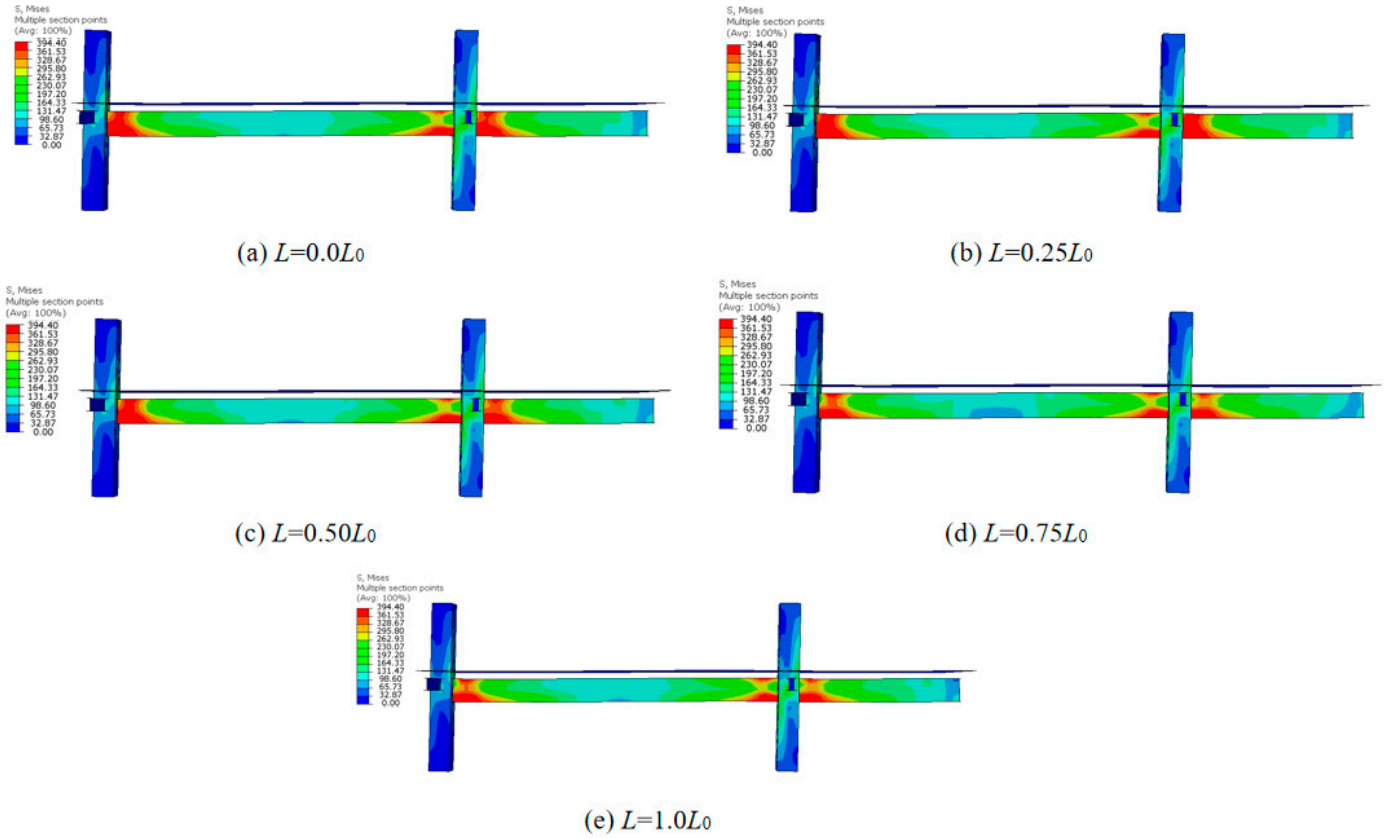

Figure 12. Stress cloud distributions in the composite frame for varying L values.

Figure 13 illustrates the concrete damage factor nephograms for the RC slab across different L values when the structure reaches a displacement of 30.6 mm. As evident from the figure, the damage region on the reinforced concrete slab, when utilizing only traditional shear studs, predominantly spans the beam end and flanks the connectors' positions, extending longitudinally along the steel beam. As the arrangement length of the URSP connectors increases, both the extent and severity of the RC slab's cracking diminish. Remarkably, when the URSP connectors' arrangement length extends to $1.0L_0$, the RC slab directly over the connectors, along its longitudinal direction, displays no cracking whatsoever.

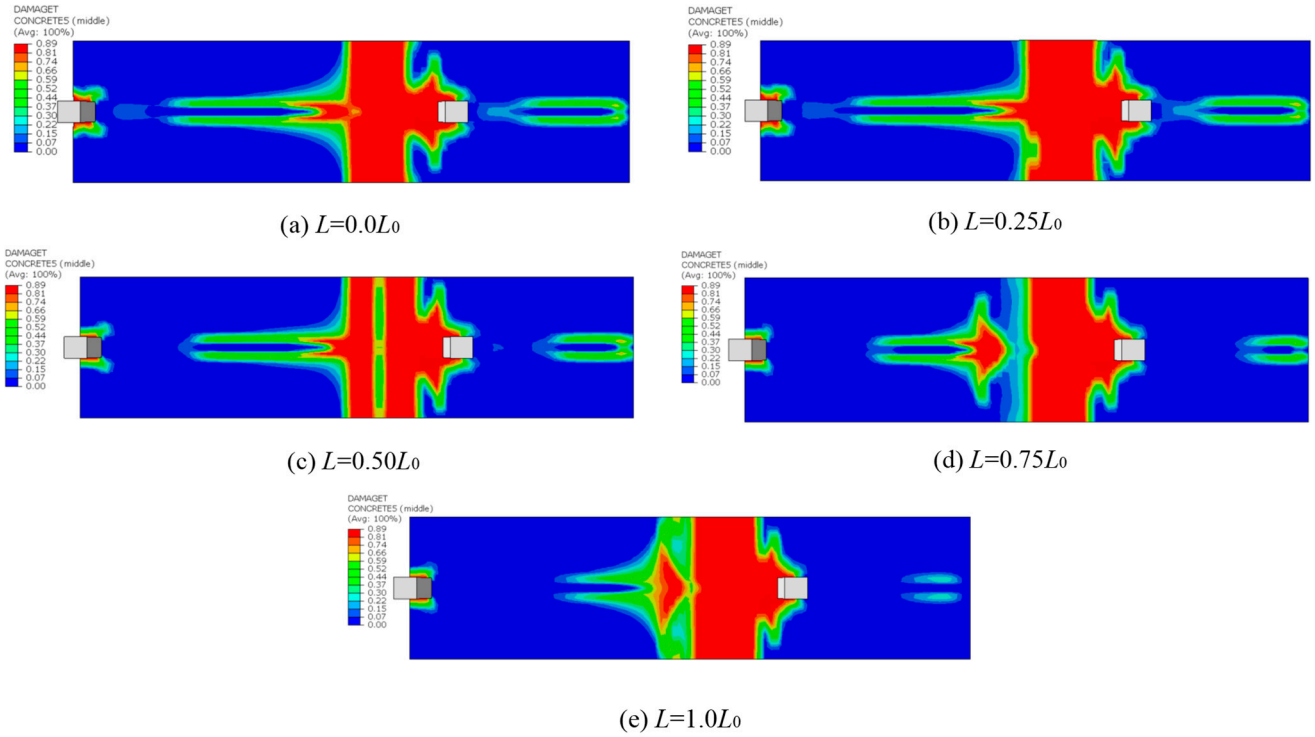

Figure 13. Concrete damage factor cloud distributions in the RC slab for varying L values.

Figure 14 presents the positive monotonic load–displacement curves for the composite frame across different L values. As observed from the figure, the progression of each curve is nearly identical. The elastic stiffness and bearing capacity derived from the load–displacement curve of the various models are compared in Table 5. When the arrangement length of the URSP connectors is less than $0.5L_0$, its increase does not noticeably impact the elastic stiffness. However, beyond this point, the elastic stiffness drops to 80% of its original value as the arrangement length extends from $0.5L_0$ to $1.0L_0$. Changes in the arrangement length do not significantly affect the bearing capacity, as both traditional shear studs and URSP connectors have the same radius, resulting in an identical ultimate shear capacity. Consequently, to enhance the anti-cracking performance while preserving the elastic stiffness, the arrangement length of the URSP connectors in the frame should be kept under $0.5L_0$.

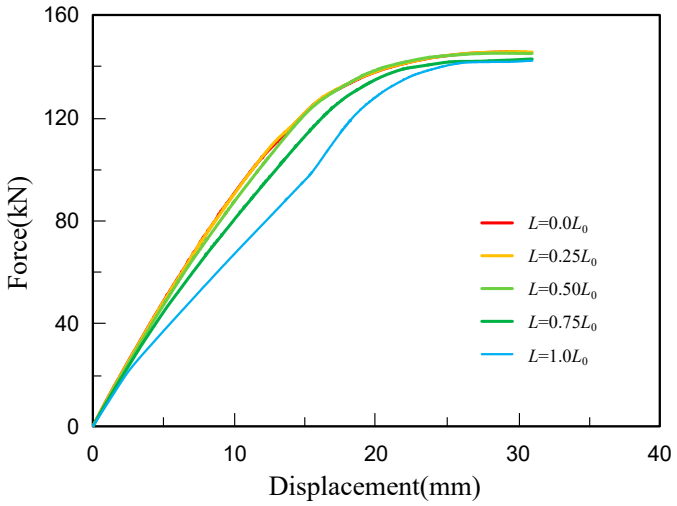

Figure 14. Numerical results comparison for models with varying L values.

Table 5. Critical mechanical parameters for model with different L values.

Arrangement Length of URSP Connectors	Initial Stiffness K_E (kN/mm)	Ultimate Load P_U (kN)	K_E/K_{E0}	P_U/P_{U0}
$0.0L_0$	11.2	145.7	1.03	1.00
$0.25L_0$	11.0	145.5	1.01	1.00
$0.50L_0$	10.8	145.0	1.00	1.00
$0.75L_0$	9.7	142.9	0.90	0.98
$1.0L_0$	8.6	142.2	0.79	0.98

Note: K_{E0} and P_{U0} denote the initial stiffness and ultimate load of CF2, respectively.

3.2. Flange Thickness of the Steel Beam

Figure 15 shows the stress distributions in the composite frame for different flange thicknesses when the frame reaches a story drift angle of 1/50. Notably, variations in flange thickness do not substantially alter the stress distribution within the steel beam. However, stress within the joint core considerably intensifies with increasing flange thickness. Once the flange thickness reaches $2.0t_w$, the steel tube in the middle column begins to yield. Figure 16 contrasts the damage levels within the RC slab for structures with different flange thicknesses. While flange thickness changes do not significantly influence the damage extent in the RC slab, the severity of cracking in the RC slab visibly diminishes as flange thickness grows.

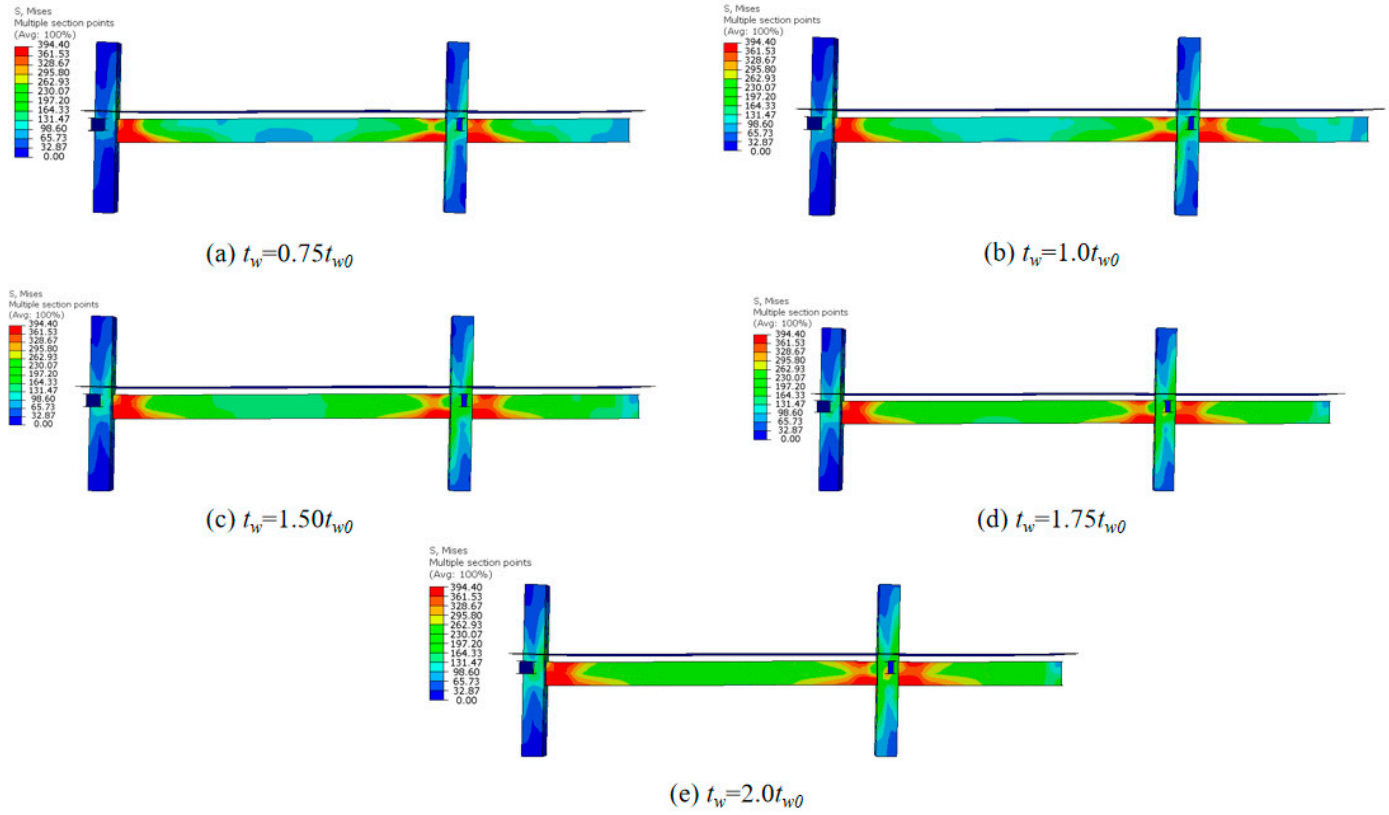

Figure 15. Stress clouds of composite frame with different t_w values.

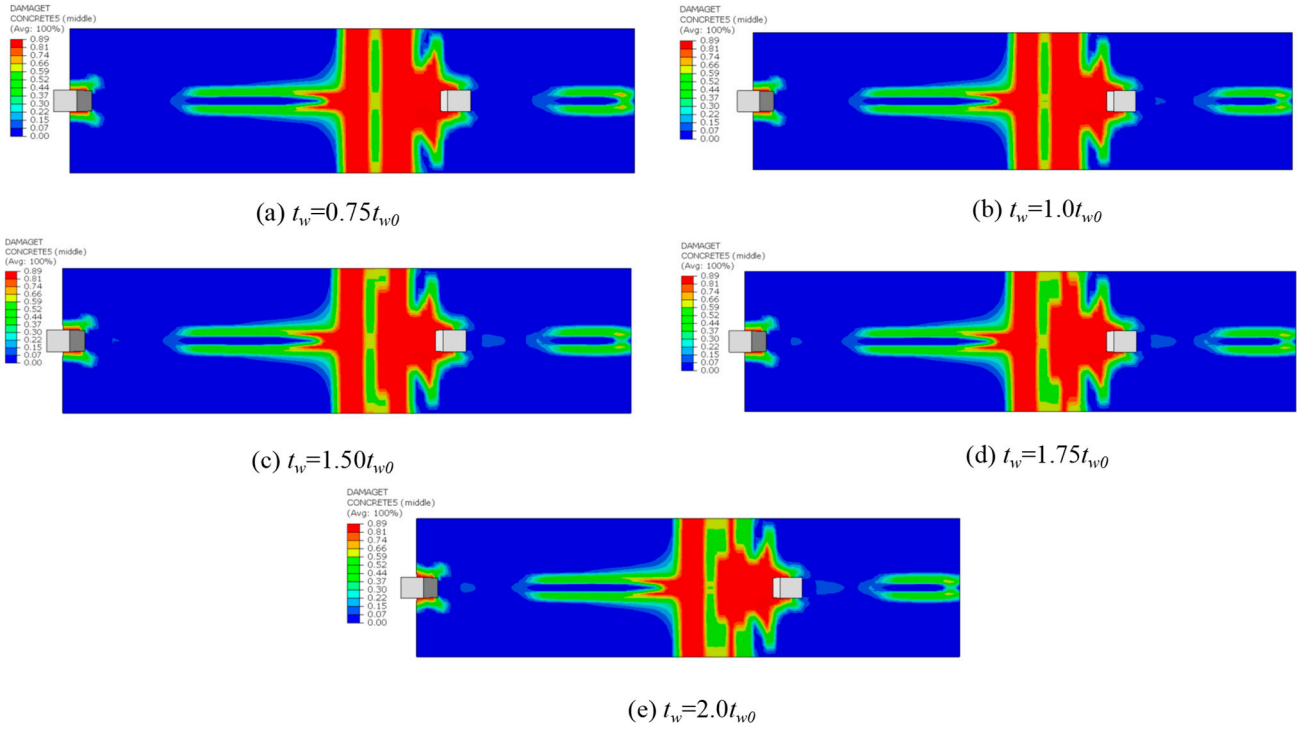

Figure 16. Concrete damage factor nephograms of RC slab with different t_w value.

Figure 17 depicts the positive monotonic load–displacement curves of the composite frame at varying steel beam flange thicknesses, when the frame reaches a story drift angle of 1/50. Notably, each curve's progression is strikingly similar. Key mechanical parameters, such as elastic stiffness and bearing capacity derived from these load–displacement curves, are summarized in Table 6. As the flange thickness increases, there is a marked improvement in both the elastic stiffness and ultimate load. The impact of flange thickness on ultimate load is especially pronounced: when the thickness increases from 0.75t_w to 2.0t_w, the frame's bearing capacity surges to more than double its original value. Hence, to bolster the frame's seismic resilience while ensuring that the steel tube in the joint core remains elastic, it is advisable to moderately increase the flange thickness.

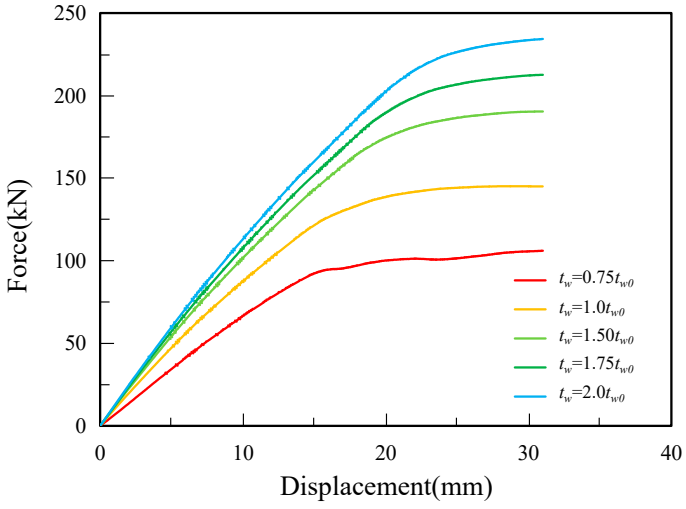

Figure 17. Comparison among the numerical results of the model with varying t_w values.

Table 6. Critical mechanical parameters of the model with different t_w values.

Flange Thickness of Steel Beam	Initial Stiffness K_E (kN/mm)	Ultimate Load P_U (kN)	K_E/K_{E0}	P_U/P_{U0}
$0.75t_{w0}$	6.6	106.0	0.61	0.75
$1.0t_{w0}$	10.8	145.0	1.00	1.00
$1.5t_{w0}$	11.7	190.4	1.08	1.31
$1.75t_{w0}$	11.8	212.6	1.09	1.45
$2.0t_{w0}$	12.3	234.3	1.14	1.62

Note: K_{E0} and P_{U0} denote the initial stiffness and ultimate load of CF2, respectively.

3.3. Steel Beam Height

Figure 18 illustrates the stress clouds of the composite frame when the steel beam height varies, observed at a displacement of 30.6 mm. The region near the beam's end has reached the yield stage. As the steel beam height increases, both the yield area near the beam's end and the stress level of the rectangular steel tube in the CFST column expand until the beam height reaches $1.0h_0$. Beyond this point, changes in the steel beam height do not noticeably affect the frame's stress distribution and levels. Figure 19 offers a comparative analysis of the damage to the RC slab of the composite frame with differing steel beam heights. While the variation in steel beam height does not notably impact the damage area of the RC slab, the extent of slab cracking consistently reduces as the steel beam height increases.

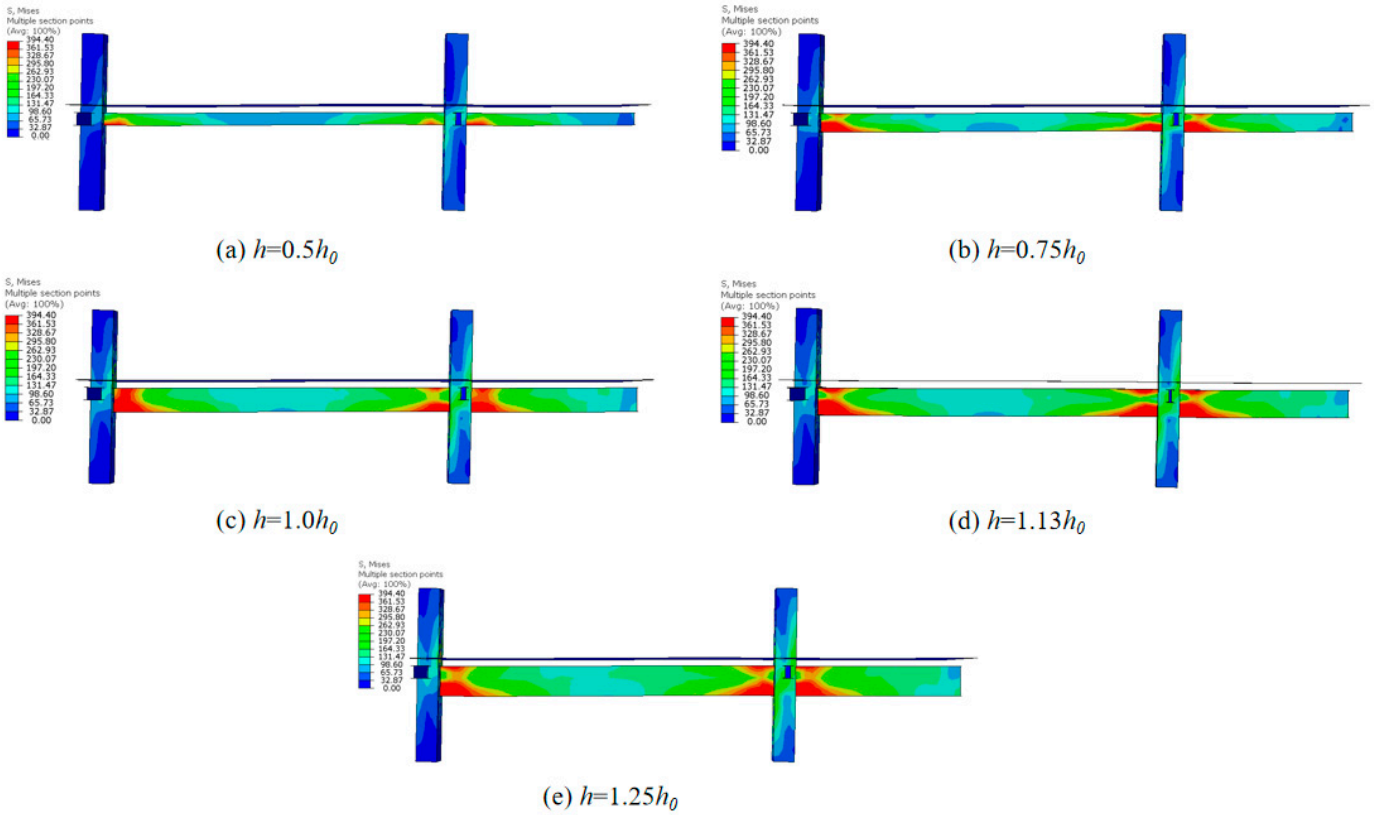

Figure 18. Stress clouds of composite frame with varying h values.

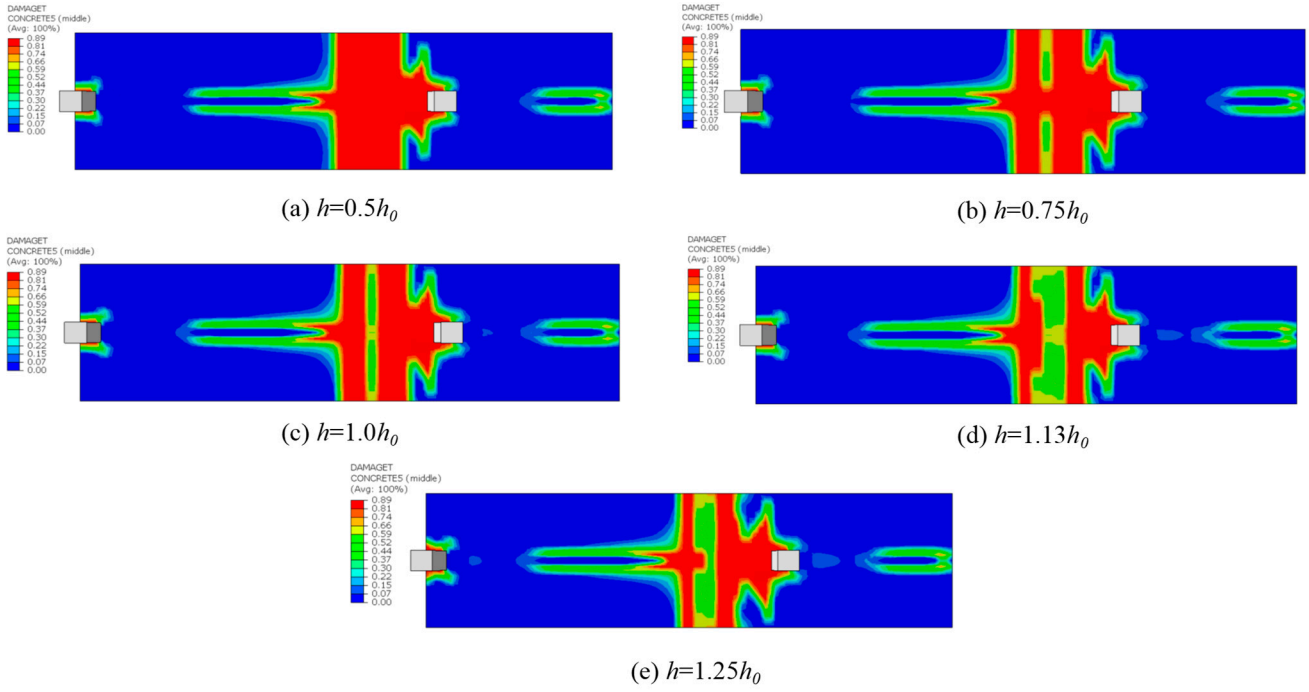

Figure 19. Concrete damage factor nephograms for the RC slab with different h values.

Figure 20 presents the positive monotonic load–displacement curves of the composite frame with varying steel beam heights, observed when the frame attains a story drift angle of 1/50. As depicted in the figure, the progression of each curve is nearly identical. Table 7 compares the elastic stiffness and bearing capacity derived from the load–displacement curve of each model. The figure demonstrates that as the steel beam height increases, both the elastic stiffness and the ultimate load of the composite also increase. Moreover, their rate of change is largely consistent. Hence, to enhance the seismic performance of the composite frame, the height of the steel beam should be increased.

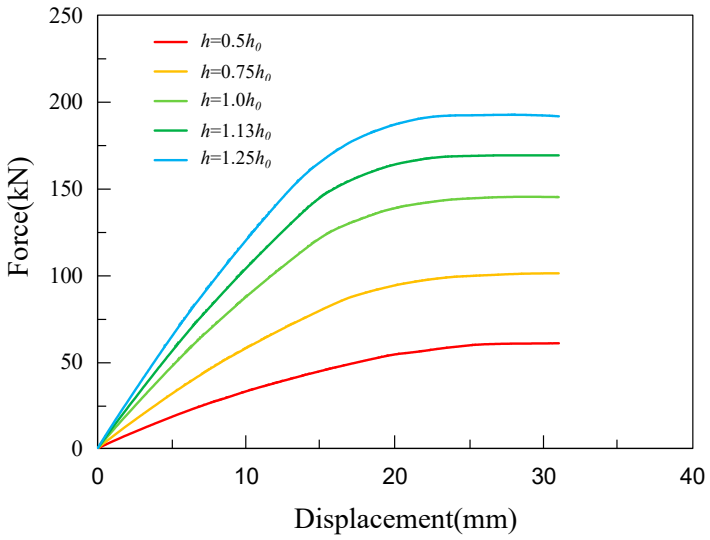

Figure 20. Comparison of the numerical results of the model with varying h values.

Table 7. Critical mechanical parameters of the model with different h values.

Steel Beam Height	Initial Stiffness K_E (kN/mm)	Ultimate load P_U (kN)	K_E/K_{E0}	P_U/P_{U0}
$0.5h_0$	4.1	60.6	0.37	0.42
$0.75h_0$	7.0	101.0	0.65	0.70
$1.0h_0$	10.8	145.0	1.00	1.00
$1.13h_0$	12.1	169.1	1.12	1.16
$1.25h_0$	14.0	191.6	1.30	1.32

Note: K_{E0} and P_{U0} denote the initial stiffness and ultimate load of CF2, respectively.

4. Conclusions

In this research, we have articulated a sophisticated finite-element model, employing a nuanced integration of shell-solid elements, facilitated through the FEM software,(Abaqus 2016) Abaqus. This model is meticulously crafted to encapsulate the intricate mechanical behaviors exhibited by shear connectors within composite frames that are fortified with URSP connectors. The veracity of this finite-element model was rigorously ascertained by a comparative analysis with experimental data, affirming a commendable level of precision and reliability. Furthermore, we meticulously examined the impact of essential design parameters, namely, arrangement length of URSP connectors, flange thickness of steel beam, and steel beam height on seismic behavior and provided value recommendations for each. The primary conclusions drawn from this study are as follows:

1. The presented shell-solid FEM model, which takes into account the intricate mechanical behavior of the shear connectors, can adeptly reproduce the nonlinear mechanical responses of the composite frame with URSP connectors. A substantial agreement between the simulation outcomes and experimental data was observed, especially concerning damage patterns, crack distributions, and hysteresis loops.
2. Evaluating key design parameters, such as the arrangement length of URSP connectors, flange thickness, and steel beam height, reveals the following:
    i. To preserve the lateral elastic stiffness and bolster anti-cracking prowess, the span for arranging URSP connectors should not exceed half of the frame beam's span.
    ii. Augmenting the flange thickness of the steel beam notably fortifies the elastic stiffness, ultimate load, and anti-cracking capability of the composite frame using URSP connectors. However, excessive flange thickness could cause the steel tube of the columns to yield.
    iii. Elevating the steel beam height markedly affects the elastic stiffness and ultimate load, with their change rates being nearly congruent. As the steel beam height expands from $0.5h_0$ to $1.25h_0$, both parameters increase to more than triple their initial values, and the cracking extent in the RC slab diminishes significantly.
3. The model proposed in this study is tailored for composite frames equipped with screw-type URSP connectors. However, to ensure comprehensive applicability, further validation and research are essential to examine the influence of different types of URSP connectors on seismic performance.

Author Contributions: Conceptualization, Z.W. and L.D.; methodology, J.Z.; software, W.W.; validation, W.W., X.N. and Z.W.; formal analysis Z.W.; investigation Z.W. and L.D.; resources, X.N.; data curation, J.Z.; writing—original draft preparation, Z.W.; writing—review and editing, L.D.; visualization, J.Z.; supervision, X.N.; project administration, L.D.; funding acquisition, X.N. and L.D. All authors have read and agreed to the published version of the manuscript.

Funding: This research was financially supported by the Original Exploration Project of the National Natural Science Foundation of China (Grant No. 52250003) and the National Natural Science Foundation of China (Grant No. 52108153).

Data Availability Statement: Data, models, or code that substantiate the findings of this study can be obtained from the corresponding author upon reasonable inquiry.

Acknowledgments: The authors express their profound gratitude for the financial backing granted by the National Natural Science Foundation of China (Grant No. 52250003 and Grant No. 52108153).

Conflicts of Interest: The authors confirm no existing conflict of interest.

References

1. Bursi, O.S.; Sun, F.F.; Postal, S. Non-linear analysis of steel-concrete composite frames with full and partial shear connection subjected to seismic loads. *J. Const. Steel Res.* **2005**, *61*, 67–92. [CrossRef]
2. Elghazouli, A.Y.; Castro, J.M.; Izzuddin, B. Seismic performance of composite moment-resisting frames. *Eng. Struct.* **2008**, *30*, 1802–1819. [CrossRef]
3. Nakashima, M.; Matsumiya, T.; Suita, K.; Zhou, F. Full-Scale Test of Composite Frame under Large Cyclic Loading. *J. Struct. Eng.* **2007**, *133*, 297–304. [CrossRef]
4. Nie, J.G.; Tao, M.X. Slab spatial composite effect in composite frame systems. I: Effective width for ultimate loading capacity. *Eng. Struct.* **2012**, *38*, 171–184. [CrossRef]
5. Zhao, H.; Tao, M.-X.; Ding, R. Experimental study on seismic behaviour of composite frames with wide floor slabs considering the effect of floor loads. *Eng. Struct.* **2020**, *220*, 111024. [CrossRef]
6. Huang, Y. Experimental Research and Analytical Modeling on the Behavior of Steel-Concrete Composite Frames. Ph.D. Thesis, Tsinghua University, Beijing, China, 2008. (In Chinese)
7. Tao, M.-X. Slab Spatial Composite Effect of Steel-Concrete Composite Frame Structural Systems. Ph.D. Thesis, Tsinghua University, Beijing, China, 2012. (In Chinese)
8. Ryu, H.-K.; Chang, S.-P.; Kim, Y.-J.; Kim, B.-S. Crack control of a steel and concrete composite plate girder with prefabricated slabs under hogging moments. *Eng. Struct.* **2005**, *27*, 1613–1624. [CrossRef]
9. He, J.; Liu, Y.; Chen, A.; Yoda, T. Experimental study on inelastic mechanical behaviour of composite girders under hogging moment. *J. Cons. Steel Res.* **2010**, *66*, 37–52. [CrossRef]
10. Chen, S. Experimental study of prestressed steel–concrete composite beams with external tendons for negative moments. *J. Constr. Steel Res.* **2005**, *61*, 1613–1630. [CrossRef]
11. Lou, T.; Karavasilis, T.L. Numerical assessment of the nonlinear behavior of continuous prestressed steel-concrete composite beams. *Eng. Struct.* **2019**, *190*, 116–127. [CrossRef]
12. Nie, J.-G.; Tao, M.-X.; Nie, X.; Fan, J.-S.; Zhang, Z.; Tang, H.; Zhu, L.; Li, Y. New technique and application of uplift-restricted and slip-permitted connection. *China Civ. Eng. J.* **2015**, *48*, 7–14, 58. (In Chinese)
13. Nie, J.; Wang, J.; Gou, S.; Zhu, Y.; Fan, J. Technological development and engineering applications of novel steel-concrete composite structures. *Front. Struct. Civ. Eng.* **2019**, *13*, 1–14. [CrossRef]
14. Vasdravellis, G.; Valente, M.; Castiglioni, C.A. Behavior of exterior partial-strength composite beam-to-column connections: Experimental study and numerical simulations. *J. Cons. Steel Res.* **2009**, *65*, 23–35. [CrossRef]
15. Vasdravellis, G.; Valente, M.; Castiglioni, C.A. Dynamic response of composite frames with different shear connection degree—ScienceDirect. *J. Cons. Steel Res.* **2009**, *65*, 2050–2061. [CrossRef]
16. Nie, J.-G.; Li, Y.-X.; Tao, M.-X. Slip performance and hysteresis model of a new type of uplift restricted-slip free connectors. *Eng. Mech.* **2014**, *31*, 46–52. (In Chinese)
17. Nie, J.-G.; Li, Y.-X.; Tao, M.-X.; Nie, X. Uplift-Restricted and Slip-Permitted T-Shape Connectors. *J. Bridg. Eng.* **2015**, *20*, 04014073. [CrossRef]
18. Nie, J.-G.; Li, Y.-X.; Tao, M.-X.; Zhang, Z.-X.; Tang, H.-Y. Experimental research on uplift performance of a new type of Uplift restricted-slip free connector. *China J. Hwy Trans.* **2014**, *27*, 38–45. (In Chinese)
19. Nie, X.; Nie, J.-G.; Tao, M.-X.; Fan, J.-S.; Tang, H.-Y. Study on steel-concrete continuous composite bridge connected by new type of steel-concrete connector without shear resistance. *J. Harbin Inst. Technol.* **2012**, *44*, 95–100. (In Chinese)
20. Han, S.-W. Experimental Study on Steel-Concrete Composite Beam with Uplift-Restricted and Slip-Permitted Connectors. Master's Thesis, Tsinghua University, Beijing, China, 2016. (In Chinese)
21. Li, Z.; Ma, X.; Fan, J.; Nie, X. Overhanging Tests of Steel–Concrete Composite Girders with Different Connectors. *J. Bridg. Eng.* **2019**, *24*, 04019098. [CrossRef]
22. Ma, X.-W. Structural System and Composite Grider Behavior of Multi-Span Suspension Bridges. Ph.D. Thesis, Tsinghua University, Beijing, China, 2016. (In Chinese).
23. Nie, X.; Duan, L.; Tao, M.; Guo, Y. Experimental investigation on the behavior of the steel-concrete composite frames with uplift-restricted and slip-permitted screw-type (URSP-S) connectors. *Eng. Struct.* **2022**, *254*, 113868. [CrossRef]
24. Zhuang, L.-D.; Zhao, J.-Z. Numerical Study on the Seismic Behavior of Eccentrically Braced Composite Frames with a Vertical Low-Yield-Point Steel Shear Link. *Buildings* **2022**, *12*, 1359. [CrossRef]
25. Zhao, J.-Z.; Zhou, Q.-L.; Tao, M.-X. Effective slab width for beam-end flexural strength of composite frames with circular-section columns. *J. Constr. Steel Res.* **2020**, *174*, 106309. [CrossRef]

26. Duan, L.; Nie, X.; Ding, R.; Zhuang, L. Research on Application of Uplift-Restricted Slip-Permitted (URSP) Connectors in Steel-Concrete Composite Frames. *Appl. Sci.* **2019**, *9*, 2235. [CrossRef]
27. Ollgaard, J.G.; Slutter, R.G.; Fishe, J.W. Shear strength of stud connectors in lightweight and normal-weight concrete. *AISC Eng. J. Am. Inst. Steel Constr.* **1971**, *169*, 55–64.
28. *JGJ138-2016*; Code for Design of Composite Structures. China Architecture & Building Press: Beijing, China, 2016. (In Chinese)
29. Esmaeily, A.; Xiao, Y. Behavior of Reinforced Concrete Columns Under Variable Axial Loads: Analysis. *ACI Struct. J.* **2005**, *102*, 736–744. [CrossRef]
30. Tao, M.-X.; Nie, J.-G. Influence of material uniaxial hysteretic laws on nonlinear analysis of composite structural members. *J. Building Struct.* **2014**, *35*, 24–32. (In Chinese)
31. Légeron, F.; Paultre, P.; Mazars, J. Damage Mechanics Modeling of Nonlinear Seismic Behavior of Concrete Structures. *J. Struct. Eng.* **2005**, *131*, 946–955. [CrossRef]
32. Lei, T.; Qian, J.; Liu, C.-Q. Application of damaged plasticity model for concrete. *Struct. Eng.* **2008**, *24*, 22–27. (In Chinese)
33. Han, L.-H.; Feng, J.-B. Constitutive relations of concrete and its applications in the integral analysis of concrete filled steel tube. *J. Harbin Uni Arch. Eng.* **1995**, *28*, 26–32. (In Chinese)
34. Han, L.-H.; Yao, G.-H.; Tao, Z. Performance of concrete-filled thin-walled steel tubes under pure torsion. *Thin-Walled Struct.* **2007**, *45*, 24–36. [CrossRef]
35. *GB50010-2010*; Code for Design of Concrete Structures. China Architecture & Building Press: Beijing, China, 2010. (In Chinese)
36. Kassem, M.M.; Nazri, F.M.; Farsangi, E.N.; Ozturk, B. Improved Vulnerability Index Methodology to Quantify Seismic Risk and Loss Assessment in Reinforced Concrete Buildings. *J. Earthq. Eng.* **2021**, *26*, 6172–6207. [CrossRef]
37. Kassem, M.M.; Nazri, F.M.; Farsangi, E.N.; Ozturk, B. Development of a uniform seismic vulnerability index framework for reinforced concrete building typology. *J. Build. Eng.* **2022**, *47*, 103838. [CrossRef]
38. *GB50011-2011*; Code for Seismic Design of Buildings. China Architecture & Building Press: Beijing, China, 2010. (In Chinese)